



MoS₂ quantum dots-interspersed Bi₂WO₆ heterostructures for visible light-induced detoxification and disinfection

Xiangchao Meng, Zizhen Li, Haoming Zeng, Jie Chen, Zisheng Zhang*

Department of Chemical and Biological Engineering, University of Ottawa, Ottawa, Ontario, K1N 6N5, Canada

ARTICLE INFO

Article history:

Received 8 November 2016

Received in revised form 27 February 2017

Accepted 28 February 2017

Available online 1 March 2017

Keywords:

Photocatalysis

Bi₂WO₆

MoS₂

Quantum dot

ABSTRACT

MoS₂ Quantum dots-interspersed Bi₂WO₆ heterostructure is fabricated for photocatalytic applications for the first time. It exhibits enhanced visible light-driven photocatalytic detoxification and disinfection in wastewater compared to bare Bi₂WO₆ and MoS₂. MoS₂ quantum dots as a co-catalyst applied in photocatalysis oxidation possesses multiple merits: (1) noble-metal-free; (2) high mobility of photogenerated charge carriers; (3) high adsorption capacity and (4) improved capture capacity of visible light photons. Electron-hole separation rate which is critical for an efficient photocatalysis is greatly improved via the built-in electric field of *p-n* heterostructure and the quantum dots interspersed on the surface. This work shed a light on loading MoS₂ quantum dots as a co-catalyst on a support aiming to significantly improve its photocatalytic performance in organic pollutants degradation and bacteria inactivation.

© 2017 Elsevier B.V. All rights reserved.

1. Introduction

Bismuth-based (Bi-based) semiconductor photocatalysis has been extensively investigated as an advanced oxidative process in environmental remediation [1,2]. Compared to other metal oxides, the valence bands of Bi-based semiconductors consist of the hybrid orbits of not only O 2p but also the Bi 6s. The well-dispersed Bi 6s orbits facilitate the mobility of photogenerated charge carriers, and decrease the band gap value as well [3,4]. As a result, Bi-based semiconductors are usually visible light-responsive owing to the narrow band gap, such as Bi₂O₃, Bi₂S₃, Bi₂MO₆ (M=Cr, Mo and W), BiVO₄, and BiOX (X=Cl, Br and I).

Among Bi-based semiconductors, Bi₂WO₆ is reported as an effective photocatalysts for detoxification in wastewater as well as polluted air [5–8]. However, the flat energy band of Bi₂WO₆ implies the low mobility of charge carriers on either valence band or conduction band. And the charge carriers are easily recombined before react with adsorbed species to generate oxidative species. Moreover, the band gap of Bi₂WO₆ is measured as about 2.70 eV, indicating only irradiations with wavelength below 460 nm are able to trigger this photocatalysis process. To improve the capacity of capturing visible light-photons for Bi₂WO₆ will be

another issue. Approaches mainly include metal/non-metal doping [9,10] and coupling co-catalyst with narrow band gap [11,12]. The synergy effect of establishment of heterostructure between Bi-based semiconductor and other semiconductors may improve the photocatalytic activity through facilitating the separation of photogenerated charge carriers forced by the built-in electric field [4,13,14]. Various Bi₂WO₆ based heterostructures were reported, such as BiOBr-Bi₂WO₆ by our group [14], Bi₂O₃-Bi₂WO₆ [12].

Recently, alternative noble-metal-free co-catalysts such as graphene, g-C₃N₄ and MoS₂ have been rapidly developed and applied in photocatalysis [15–17]. These conductive two-dimensional (2D) nanosheets not only serve as a support to prevent agglomeration of the photocatalysts, but also provide charge-transfer channels with relatively high mobility to improve the photogenerated charge carriers separation efficiency [18]. Two-dimensional MoS₂ is supposed to be a promising candidate to facilitate organic degradation as a co-catalyst as well. However, it is reported that the active sites for 2D MoS₂ only located along its edges, while the basal surface of MoS₂ is catalytically inert [19]. Moreover, the semiconducting MoS₂ exhibits limited mobility for charge transport [20]. Even though two-dimensional MoS₂-Bi₂WO₆ core-shell heterostructure was reported with enhanced photocatalytic activity in degradation of methylene blue [21]. That might be attributed to the enhanced adsorption capacity by the introduction of MoS₂ sheets on Bi₂WO₆. The MoS₂-Bi₂WO₆ direct heterojunctions were also fabricated by one-step hydrothermal method and demonstrated impressive visible-light-driven photocatalytic activity [22]. However, the large size of MoS₂ may not

* Corresponding author.

E-mail addresses: xmeng086@uottawa.ca (X. Meng), zli125@uottawa.ca (Z. Li), hzeng047@uottawa.ca (H. Zeng), jchen342@uottawa.ca (J. Chen), zzhang@uottawa.ca (Z. Zhang).

overcome the shortages as mentioned above as only the edges of MoS₂ are active and the extent of activity enhancement will therefore be limited. It is reported that MoS₂ quantum dots (QDs) can be prepared by a bath sonication process [23]. MoS₂ QDs as a co-catalyst may overcome these above mentioned limitations, especially the active sites only located at the edges. Additionally, QDs combined on photocatalysts may provide a convenient approach to direct the flow of the photogenerated charge carriers, so as to improve theirs separation efficiency [24,25].

In this work, we demonstrate that the fabrication of MoS₂ QDs interspersed Bi₂WO₆ heterostructures via a simple bath sonication method. The MoS₂-Bi₂WO₆ composites exhibited excellent photocatalytic detoxification as well as disinfection in wastewater compared to bare Bi₂WO₆ and MoS₂. As far as we know, this is the first example of using MoS₂ QDs as a co-catalyst for photocatalytic applications.

2. Experimental

2.1. Chemicals

All chemicals were purchased from Fisher Scientific and used as received of reagent or higher purity, unless otherwise mentioned.

2.2. Synthesis of layered MoS₂ nanoflowers

The layered MoS₂ nanoflowers were synthesized via a facile hydrothermal method [26]. Typically, 1.20 g of Na₂MoO₄·2H₂O and 1.60 g of NH₂CSNH₂ were mixed together with 0.60 g of oxalic acid in 80 mL Deionized Distilled Water (DDW) termed as solution A. Solution A was magnetically stirred for 30 min, and then it was transferred into a 100-mL Teflon-lined stainless steel autoclave (Parr Instrument Company). The autoclave was heated and maintained at 180 °C for 24 h, and then naturally cooled down to room temperature. The black precipitates were separated by vacuum filtration and washed twice with DDW and once with ethanol. At last, the black precipitates were dried at 60 °C for 12 h before collected for further use.

2.3. Synthesis of hierarchical Bi₂WO₆

Hierarchical Bi₂WO₆ samples were synthesized through a template-free hydrothermal method [4]. In a typical process, 0.97 g of Bi(NO₃)₃·5H₂O were dissolved in 30 mL acetic acid, termed as solution B, which was magnetically stirred for 20 min. Then, 0.33 g of Na₂WO₄·2H₂O were dissolved in 50 mL DDW, termed solution C. Solution C was dropwise added into solution B and magnetically stirred for another 20 min before transferring into a 100-mL Teflon-lined stainless steel autoclave. The autoclave was heated at 180 °C for 20 h. After the autoclave was naturally cooled down to room temperature, the precipitates were separated by vacuum filtration and washed twice with DDW then once by ethanol. The precipitate was dried at 60 °C for 12 h before collected for further use.

2.4. Synthesis of MoS₂ QDs interspersed-Bi₂WO₆ composites

A highly dispersed suspension of MoS₂ QDs interspersed on hierarchical Bi₂WO₆ was synthesised by a simple bath sonication method [23], as schematically depicted in Fig. 1. Specifically, 0.30 g of Bi₂WO₆ and a designate amount of MoS₂ were dissolved in 40 mL ethanol. The above suspension was ultrasonicated for 2 h and then magnetically stirred until the solvent was naturally evaporated. The product was dried at 60 °C for 12 h before collected. Composites of 0.5, 1.0, 1.5 and 2.0% MoS₂ interspersed-Bi₂WO₆ composites were prepared.

2.5. Characterization

Crystal structures were measured on a Rigaku Ultima IV Diffractometer with Cu K α radiation ($\lambda = 0.15418 \text{ nm}$) at 40 kV and 44 mA. Surface composition and chemical states were performed on a XSAM-800 X-ray Photoelectron Spectroscopy (XPS). Morphologies were investigated by a field-emission scanning electron microscope (FE-SEM, JEOL JSM-7500F) and a transmission electron microscope (TEM, JEM-2100F). The specific surface area, pore volume and average pore size were obtained from N₂ sorption isotherms at 77 K, using automatic adsorption apparatus and measurement systems (ASAP 2020, Micromeritics and Nova 4200E, Quantachrome). The Brunauer, Emmett and Teller (BET) surface area of the samples were calculated using multi-point estimation. The pore volumes were calculated using the volumes of adsorbed N₂ at $p/p_0 = 0.977$. Ultraviolet-visible diffuse reflectance spectra (DRS) were detected using a Thermo Evolution 300 spectrophotometer. Electrochemical properties of prepared samples were performed on a CHI 604E electrochemical analyzer (CH Instruments Inc., USA) with a platinum wire as a counter electrode, a calomel reference electrode and a working electrode. The working electrode was composed of indium tin oxide (ITO, 75 × 25 × 1.1 mm, 15–25 Ω, Sigma-Aldrich Canada Co.), glass coated with the prepared samples. The electrochemical impedance spectroscopies (EIS) were recorded with frequencies in the range of 0.01–1,000,000 Hz and a sinusoidal wave of 5 mV. The electrolyte was Na₂SO₄ with a concentration of 0.50 mol/L.

2.6. Photocatalytic activity tests

2.6.1. Adsorption and degradation of rhodamine B (RhB)

The adsorption capacity for Bi₂WO₆, MoS₂ and MoS₂-Bi₂WO₆ composites were measured via adsorbing RhB in dark. In each test, 0.10 g of photocatalysts were mixed with 100 mL of RhB solution with initial concentration of 10 mg/L (catalysts dosage: 1.0 g/L). The suspension was magnetically stirred for 60 min and temperature of the reacting system was kept at 20 °C. Aliquots were drawn at every 10 min. After centrifuging at 13,000 rpm for 5 min, the supernatant was analyzed using a spectrometer (Genesys 10 UV) with wavelength fixed at 554 nm which is the characteristic peak location of RhB. The concentration of RhB can be determined based on Beer-Lambert Law. The sorption capacity, q_t [mg_{RhB}/g_{cat.}] of the composite powders can be computed by Eq. (1) as follows,

$$q_t = \frac{(c_0 - c_t) \times V}{m} \quad (1)$$

where c_0 and c_t [mg/L] are the solution concentrations of RhB at initial and time t (min), respectively; V [L] and m [g] represent the volume and the catalyst weight in the reacting system.

The photocatalytic activity of prepared sample was investigated with regards to RhB under visible light irradiation. Specifically, a 500-mL beaker with a cooling jacket to maintain the temperature at 20 °C served as the reactor. The visible light source was a 300-W halogen tungsten projector lamp (Ushio) with a UV cut-off (Kenko Zeta, transmittance >90%) to filter out the incident irradiation with wavelength below 410 nm. Intensity of irradiation on the surface of the solution was measured to be 1.1×10^{-2} Einsteins $\text{m}^{-2} \text{s}^{-1}$ through a quantum meter (Biospherical QSL-2100, 400 < λ < 700 nm). In each batch, 0.10 g of photocatalysts were added into 100 mL of RhB solution with concentration of 10 mg/L. The lamp turned on after 30 min, and the test carried out lasted for 90 min. Aliquots were taken and tested with same procedure in the adsorption test. Total organic carbon (TOC) was measured by an Apollo 9000 TOC analyzer equipped with a Non-Dispersive Infra-Red (NDIR) detector. The combustion temperature was fixed

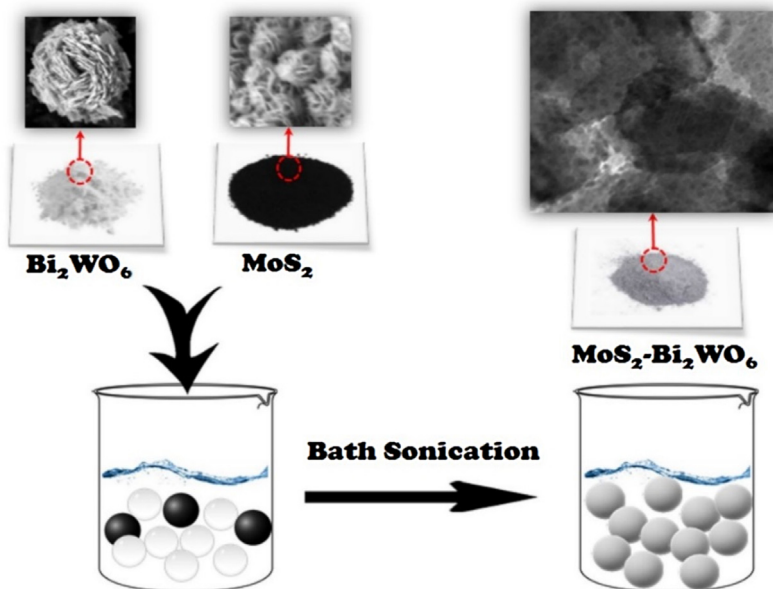


Fig. 1. Schematic preparation of MoS₂ QDs-interspersed Bi₂WO₆ composites via a bath sonication method.

at 750 °C. Samples taken at time of 0, 30, 60 and 90 min were investigated.

Reusability of 1.0% MoS₂-Bi₂WO₆ composite was tested with regard to RhB for four runs under visible light irradiation. Typically, photocatalysts were separated out by centrifugation between two runs and then remixed with fresh RhB solution with initial concentration of 10 mg/L in the following experiment without a wash.

2.6.2. Temporal course of inactivation

Wild-type *Escherichia coli* (*E. coli*) K-12 (TG1 strain), a non-pathogenic and common model, was used as a standard strain for the bacterial inactivation studies. All inactivation trials were performed in triplicate, and all materials were sterilized for 20 min at 121 °C prior to use. Cell culture were prepared by growing *E. coli* K-12 (TG1) aerobically in Luria-Bertani medium (Difco LB broth, Miller; composition: 10 g/L tryptone, 5 g/L yeast extract and 10 g/L NaCl) on a rotary shaker at speed of 250 rpm and temperature of 37 °C for 18 h until the stationary phase was reached. The cell concentration was determined by serial dilution and plating. For the enumeration, 25 µL of cell solution were spread on LB agar plates and incubated at 37 °C for 18 h. Standard plate counts for viable and cultivable bacteria was used for enumeration [27]. In each temporal course of inactivation, 0.10 g of photocatalysts were dispersed in 100 mL of saline solution containing 10⁶ CFU (colony forming units)/mL *E. coli* K-12 (TG1). After magnetically stirring for 30 min in dark, the suspension was illuminated for 60 min. The temperature of the system was kept at 20 °C using a water bath. Aliquots were drawn, and serially diluted in saline solution and spread onto LB agar plates. The plates were then incubated at 37 °C for 18 h and enumerated. To study the bacterial regrowth after photocatalytic oxidation, treated waters were stored for 3 days. The number of bacteria was also enumerated as mentioned above.

2.7. Electronic structure calculation

The quantum-mechanical calculations were performed on the basis of density functional theory (DFT) [28]. The generalized gradient approximation (GGA) was applied to exchange-correlation effects. The open access software Quantum ESPRESSO was used, which utilizes pseudopotentials to describe electron-ion interac-

tions and represents electronic wave functions using a plane-wave basis set [29]. The kinetic energy cut-off was set to 300 eV.

3. Results and discussions

3.1. Crystal structure and surface composition analysis

The XRD patterns (Fig. 2) for pure Bi₂WO₆ agree well with an orthorhombic crystal structure (space group: pbca (61), PDF card number 39-0256) [30]. All of the characteristic peaks were identified. For pure MoS₂, all the diffraction peaks can be indexed to the hexagonal phase of MoS₂ (space group: P-6m2 (187), PDF card number: 24-0513) [31]. However, the weak peaks for MoS₂ suggest its poor crystallinity. Major peaks at 2θ of 14.4°, 32.6° and 58.2° may be attributed to the (002), (100) and (110) planes of MoS₂. For MoS₂-Bi₂WO₆ composites, however, no peaks for MoS₂ were found due to its low contents in the composites. And no peaks shift for Bi₂WO₆ were observed, indicating the introduction of MoS₂ has negligibly affected the crystal structure of Bi₂WO₆. The Crystal sizes and lattice parameters were also calculated (Table 1). The crystal size for pure Bi₂WO₆ is 211 Å, that for MoS₂ doped Bi₂WO₆ is in the range of 210–214 Å. Lattice parameters for pure Bi₂WO₆ are $a = 5.4499$, $b = 16.3616$, $c = 5.4842$, and the introduction of MoS₂ negligibly influence the lattice parameters for pure Bi₂WO₆. These results indicate that loading of MoS₂ quantum dots may not destroy the crystal structure of Bi₂WO₆ during the bath sonication process, and MoS₂ were possibly just resting on the surface as opposed to covalently anchoring to the lattice of Bi₂WO₆ [32].

To further probe the chemical states and composition of MoS₂-Bi₂WO₆ composites, XPS was employed and results including a survey spectrum and high-resolution orbit scans were shown in Fig. 3. All spectra were calibrated with C 1s, the binding energy of which is fixed at 284.6 eV. In the XPS survey spectrum (Fig. 3a), all component elements (i.e. Bi, W, O, Mo and S) for MoS₂-Bi₂WO₆ composites were detected and identified, no impurity peaks were found. In the high-resolution Mo 3d orbit scan (Fig. 3b), two peaks located at binding energies of 226.5 and 230.0 eV may be assigned to Mo 3d doublets, namely 3d_{3/2} and 3d_{5/2} [33]. A small peak at binding energy of 226.3 eV may be assigned to S 2s. For the high-resolution scan of S 2p orbit, two doublets peaks were observed. Specifically, peaks located at binding energy of 164.1 eV may be

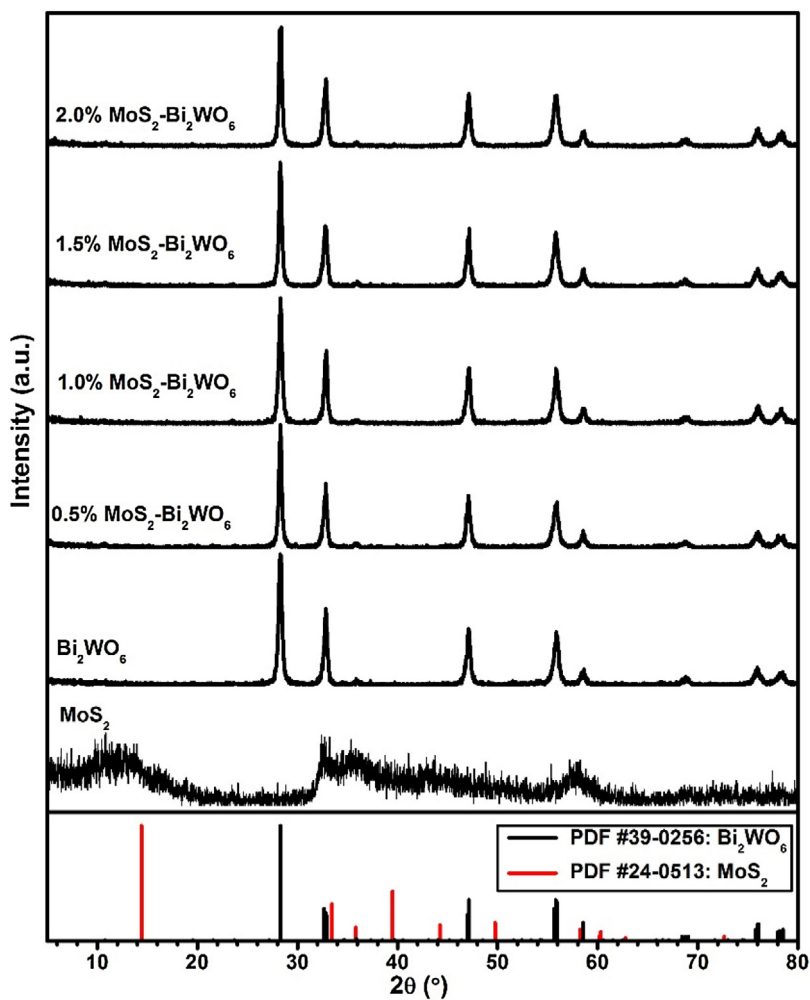


Fig. 2. XRD patterns of prepared samples, and standard XRD patterns for pure Bi₂WO₆ (PDF card # 39-0256) and MoS₂ (PDF card # 24-0513).

Table 1
Crystal size and lattice parameters of prepared samples.

Composites	Crystal size (Å)	Lattice parameters (Å)		
		a	b	c
Bi ₂ WO ₆	211	5.4499	16.3616	5.4842
0.5%MoS ₂ -Bi ₂ WO ₆	212 (+0.47%)	5.4535 (+0.07%)	16.3975 (+0.22%)	5.4656 (-0.34%)
1.0%MoS ₂ -Bi ₂ WO ₆	210 (-0.47%)	5.4522 (+0.04%)	16.4157 (+0.33%)	5.4497 (-0.63%)
1.5%MoS ₂ -Bi ₂ WO ₆	213 (+0.95%)	5.4580 (+0.15%)	16.3540 (-0.05%)	5.4650 (-0.35%)
2.0%MoS ₂ -Bi ₂ WO ₆	214 (+1.42%)	5.4551 (+0.10%)	16.3824 (+0.13%)	5.4737 (-0.19%)

attributed to Bi 4f_{5/2} with a trivalent oxidation state. Two small doublets adjacent to Bi 4f_{5/2} at binding energy of 167.0 and 165.8 eV can be assigned to S 2p_{1/2} and S 2p_{3/2} respectively [34]. The Mo 3d and S 2p peaks are located the characteristic of MoS₂ with no detectable indication of Mo oxidation states other than Mo⁴⁺ or of any sulfur species other than sulfide [35]. With increase in MoS₂ content in the composite, the peak intensities for Mo and S are increased. The [S]/[Mo] ratio can be estimated via Eq. (2) as about 2.4, which is close to the stoichiometric value for MoS₂. It can concluded the presence of MoS₂ on the surface of Bi₂WO₆ with the formula of MoS₂.

$$c_i = \frac{\frac{A_i}{q_i}}{\left[\sum_{i=1}^n \frac{A_i}{q_i} \right]} \quad (2)$$

where c_i are concentrations of specie i , A_i are XPS peak areas and q_i are experimental photoionization cross sections as given by Wagner [36] for various elements present on the surface.

3.2. Morphologies

The morphologies and microstructure of pure Bi₂WO₆, MoS₂ and MoS₂-Bi₂WO₆ composites were investigated by SEM and TEM. The SEM image of pure Bi₂WO₆ shows hierarchical microsphere microstructures with diameters in the range of 1–3 μm (Fig. 4a). The thickness of the square plates (Fig. 4d) composed of the microsphere in the nano scale. The SEM image of pristine MoS₂ (Fig. 4b) exhibits microflower morphology. However, for MoS₂-Bi₂WO₆ (Fig. 4c), nanoplates were randomly stacked together. The destruction of the microflower may be resulted from the effect of sonication during the bath sonication treatment. In the TEM image

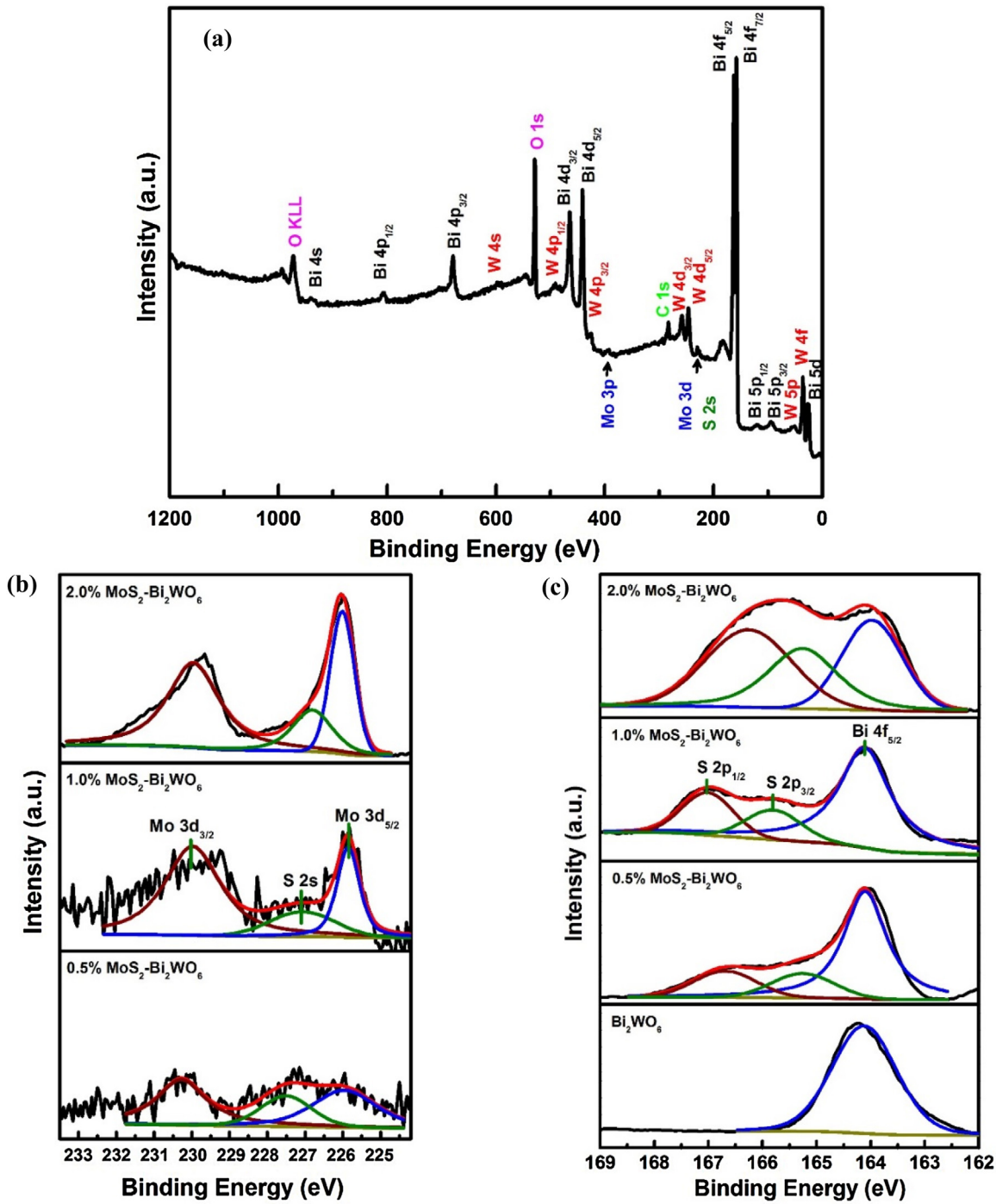


Fig. 3. XPS spectra of $\text{MoS}_2\text{-Bi}_2\text{WO}_6$ composites: (a) survey, (b) Mo 3d and (c) S 2p.

of $\text{MoS}_2\text{-Bi}_2\text{WO}_6$ composite (Fig. 4e), two-dimension nanoplates were also observed with side length of 100–400 nm. In the magnified TEM image of $\text{MoS}_2\text{-Bi}_2\text{WO}_6$ in Fig. 4f, well-dispersed quantum dots (QDs) can be found on the nanoplates. Diameter size distribution of the QDs was illustrated in the inset of Fig. 4f, they are in the range 1–9 nm and 90% of them with diameter of 1.8–5.6 nm. The lattice can be observed (Fig. 4f). Distance between two planes was measured as about 0.37 nm, which may be assigned to the (111) direction of Bi_2WO_6 based on the PDF card (#39-0256) [4].

3.3. UV-vis diffuse reflectance spectra

Optical properties of Bi_2WO_6 , MoS_2 as well as $\text{MoS}_2\text{-Bi}_2\text{WO}_6$ composites, were characterized by DRS in the range of 200–700 nm. In Fig. 5, the band gap absorption edge of Bi_2WO_6 is around 450 nm, suggesting Bi_2WO_6 is visible light-responsive. MoS_2 almost exhibits complete adsorption in both UV and visible light region, owing for its narrow band gap. Notably, with introduction of MoS_2 , the absorption intensity in the visible light region was boosted. Upon increasing the loading amount of MoS_2 in the composite, the absorption intensity in the visible light region was

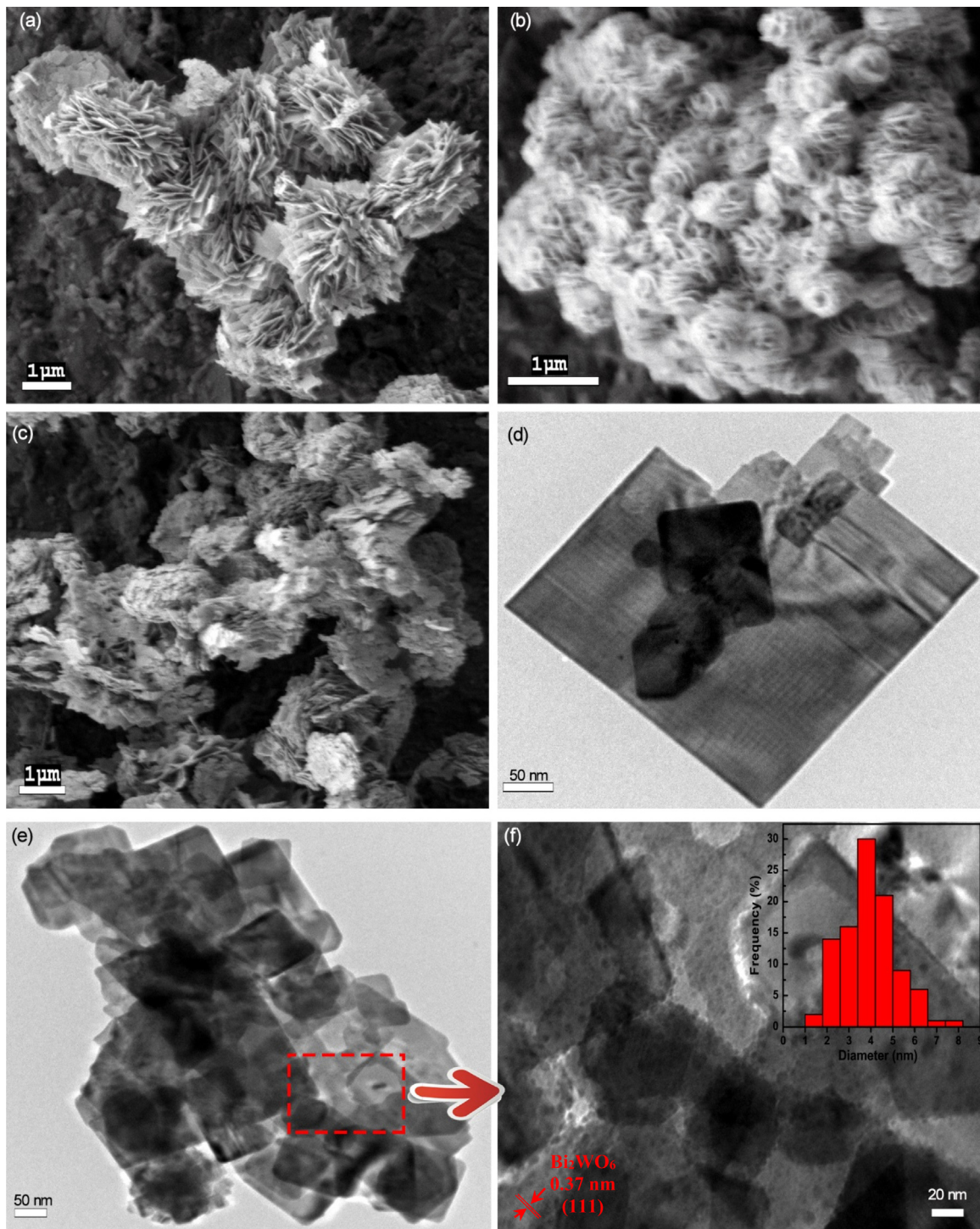


Fig. 4. SEM images of (a) pure Bi_2WO_6 , (b) pure MoS_2 and (c) MoS_2 - Bi_2WO_6 composites; and TEM images of (d) pure Bi_2WO_6 and (e, f) MoS_2 - Bi_2WO_6 composites.

gradually improved compared to the bare Bi_2WO_6 . The bandgap (E_g) of the semiconductors can be calculated by the classical Tauc approach as shown in Eq. (3):

$$\alpha E_{\text{photon}} = K(E_{\text{photon}} - E_g)^{\frac{n}{2}} \quad (3)$$

where $E_{\text{photon}} = h\nu$; α , K , E_g , n , h and ν respectively represent the absorption coefficient, constant for semiconductor (usually equal to 1), bandgap energy, constant for semiconductor depending on the type of the band gap (direct transition: $n = 1$; indirect transition:

$n = 4$, for Bi_2WO_6 , $n = 1$), Planck constant, and irradiation frequency [37]. Plots of αE_{photon} vs E_{photon} were illustrated in the inset of Fig. 5. Band gap for pure Bi_2WO_6 was about 2.70 eV. Comparatively, Band gaps for 0.5, 1.0, 1.5, and 2.0% MoS_2 - Bi_2WO_6 composites were 2.62, 2.60, 2.52 and 2.50 eV, respectively. This result indicates the band gap of MoS_2 - Bi_2WO_6 was slightly narrowed compared to bare Bi_2WO_6 . The red-shift in the DRS spectra for MoS_2 - Bi_2WO_6 may also be resulted from the narrowed band gap.

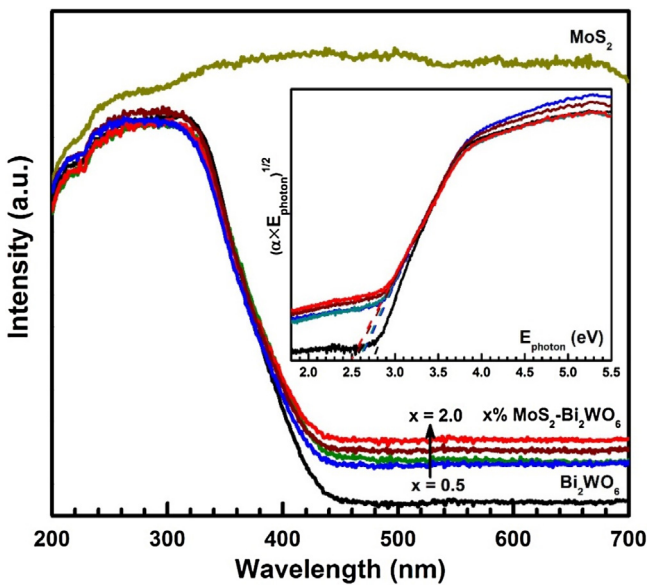


Fig. 5. UV-vis Diffuse Reflectance spectra and the plots of $(\alpha \times E_{\text{photon}})^{1/2}$ vs. E_{photon} (inset) of pure Bi_2WO_6 , MoS_2 and MoS_2 - Bi_2WO_6 composites.

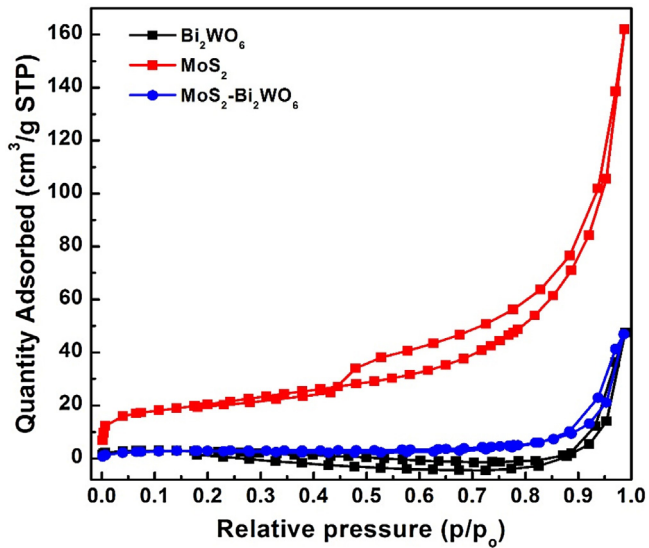


Fig. 6. N_2 sorption isotherms for Bi_2WO_6 , MoS_2 - Bi_2WO_6 and MoS_2 .

3.4. N_2 sorption isotherms

N_2 sorption isotherms were measured for pure Bi_2WO_6 , MoS_2 - Bi_2WO_6 and MoS_2 and are depicted in Fig. 6. All three isotherms are attributed to type IV physisorption isotherms [38,39]. Characteristic features of this type of isotherm are its hysteresis loop associated with capillary condensation occurring in mesopores, and the limiting uptake in the range of high relative pressure. Hysteresis loop is a H3 loop, which is mainly resulted from plate-like particles giving rise to slit-shaped pores [38–40]. This result reveals the hierarchical microsphere microstructures that were observed in the SEM images. The specific surface area as well as pore volume calculated from the isotherms are summarized in Table 2. The specific surface area of pure Bi_2WO_6 is as small as $9.4 \text{ m}^2/\text{g}$. Pure MoS_2 possesses high specific surface area of $72.0 \text{ m}^2/\text{g}$, which results in the high adsorption capacity of pure MoS_2 . Upon introduction of MoS_2 , the specific surface was slightly increased, while the pore volume was slightly decreased. The decrease in pore volume via loading MoS_2

Table 2
Specific surface area and pore volume of Bi_2WO_6 , MoS_2 - Bi_2WO_6 and MoS_2 .

Sample	S_{BET} (m^2/g)	Pore volume (cm^3/g)
Bi_2WO_6	9.4	0.074
MoS_2 - Bi_2WO_6	10.5	0.073
MoS_2	72.0	0.253

on Bi_2WO_6 may be caused by the MoS_2 quantum dots blocking the slit-like pores. The improvement of specific surface area via loading MoS_2 on Bi_2WO_6 may increase the adsorption capacity of organic pollutants in water.

3.5. Adsorption analysis

Adsorption kinetics are important for the description of solute uptake rate and for understanding dynamic sorption behavior of the system, and are strongly dependent on adsorbate-adsorbent interactions [41]. Adsorption equilibrium can describe the adsorption capacity of a material when a dynamic balance reached. The adsorption equilibrium and kinetics modelling for prepared samples were plotted in Fig. 7. In Fig. 7a, the equilibrium sorption capacity (q_e) for MoS_2 is 82.6 mg/g . Even though this value is lower than that for activated carbon (Darco G60, 100 mesh, Sigma-Aldrich) which is 219.8 mg/g , it is still undoubtedly very impressive. When MoS_2 doped on Bi_2WO_6 , q_e is gradually increased from 0.87 mg/g for

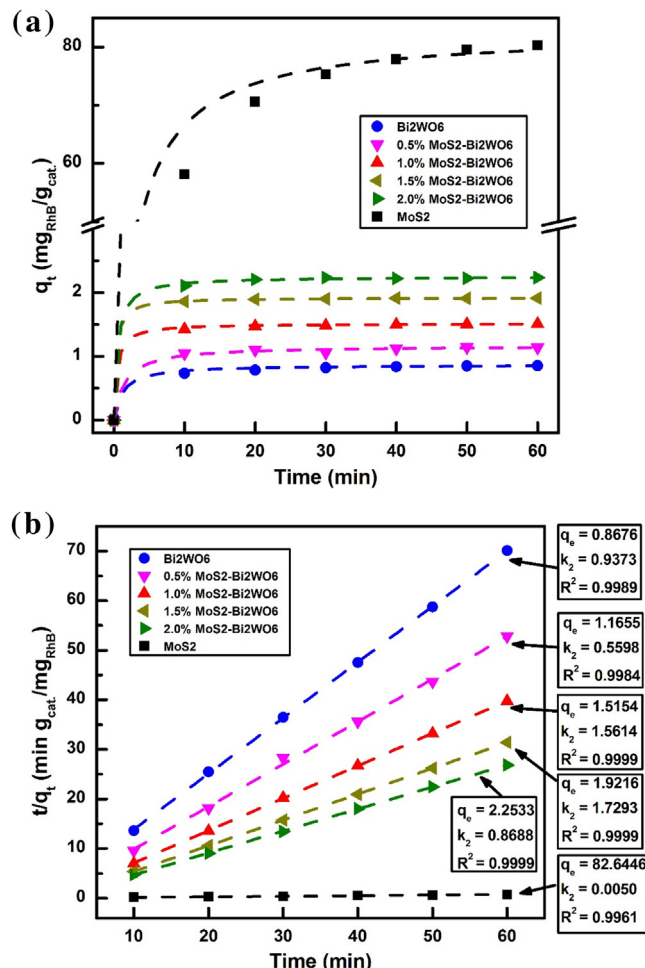


Fig. 7. (a) RhB adsorption isotherms (b) Pseudo second-order modelling for pure Bi_2WO_6 , MoS_2 - Bi_2WO_6 and MoS_2 composites, where dash lines in (a) and (b) represent Pseudo second-order modelling results and fitting lines, respectively.

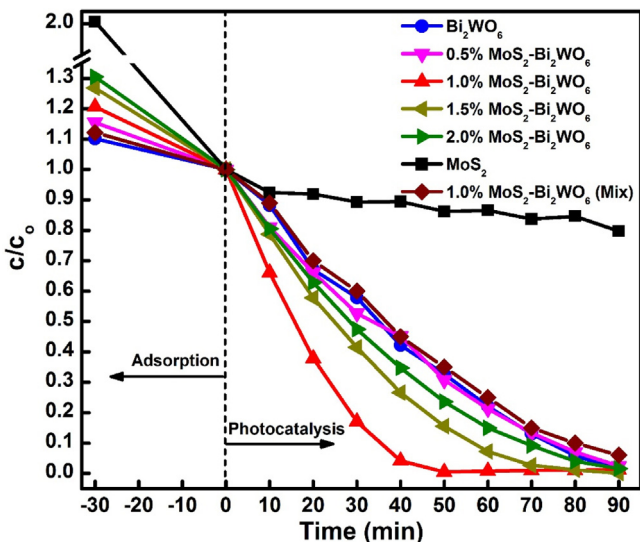


Fig. 8. Photocatalytic degradation of RhB in the presence of prepared samples under visible light irradiation. (Catalyst dosages: 1 g/L, initial concentration of RhB: 10 mg/L, Temperature: 20 °C).

pure Bi_2WO_6 to 2.25 mg/g for 2.0% MoS_2 - Bi_2WO_6 composites. The improvement for MoS_2 -doped Bi_2WO_6 in adsorption capacity may be attributed to the high adsorption capacity of MoS_2 . The adsorption kinetics can be described by a pseudo second-order model (Eq. (4)) [42]

$$\begin{aligned} \frac{dq_t}{dt} &= k_2(q_e - q_t)^2 \\ \Rightarrow \frac{t}{q_t} &= \frac{1}{k_2 q_e^2} + \frac{1}{q_e} t \end{aligned} \quad (4)$$

where k_2 is the equilibrium rate constant of pseudo second-order adsorption ($\text{g}_{\text{adsorbent}} \text{mg}_{\text{adsorbate}}^{-1} \text{min}^{-1}$). It should be notable that the fast adsorption process with high rate constant (k_2). k_2 for these three processes with pure Bi_2WO_6 and MoS_2 and MoS_2 - Bi_2WO_6 were calculated via fitting the plots of t/q_t vs t (shown in Fig. 7b). All the R^2 are almost close to 1, indicating the high appropriateness of this model to describe this process. Specifically, in presence of Bi_2WO_6 , MoS_2 - Bi_2WO_6 and MoS_2 , the k_2 for each process is shown in Fig. 7b. The adsorption rate Bi_2WO_6 is greatly improved when MoS_2 QDs loaded on its surface. The enhanced adsorption capacity and improved adsorption rate constant may be regarded as one of the reasons in the enhanced photocatalytic degradation process.

3.6. Photocatalytic activity test

3.6.1. Degradation of RhB

Activity screening for the prepared composites was performed by comparing the RhB removal observed using a photocatalysis process under visible light irradiation. The screening results are given in Fig. 8. Preliminary trials using pure MoS_2 indicated only 20% of RhB removal in 90 min under visible light irradiation, while a 99% RhB removal can be reached in 90 min when pure Bi_2WO_6 presented under visible light irradiation. A synergy effect is observed between MoS_2 and Bi_2WO_6 when they are coupled. With increase the content of MoS_2 from 0.5–1.0%, the RhB removal efficiency was significantly improved. Specifically, a complete RhB removal can be reached in 50 min in the presence of 1.0% MoS_2 - Bi_2WO_6 under visible light. However, further increase the loading amount of MoS_2 to 1.5% and even 2.0%, the photocatalytic activity of RhB removal become worse, while it is still higher than that for using bare Bi_2WO_6 . This phenomenon may be because the excessive MoS_2 QDs

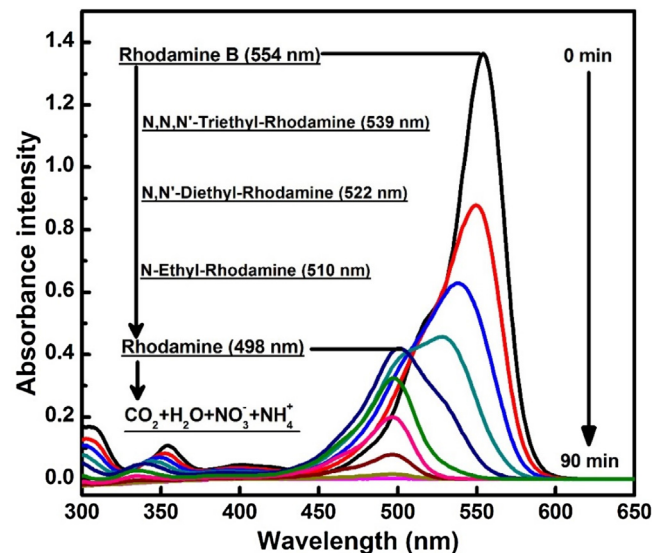


Fig. 9. UV-vis spectra of RhB samples taken during the photocatalytic process in the presence of 1.0% MoS_2 - Bi_2WO_6 .

possibly blocked the irradiation reach the surface of Bi_2WO_6 so as to the decrease the production of strong oxidative species (i.e. h^+). To further explore the synergy effect, 1.0% of MoS_2 were mechanically mixed with Bi_2WO_6 and the photocatalytic removal result is shown in Fig. 8. It turns out the RhB removal efficiency in 90 min under visible light is lightly lower than that when using bare Bi_2WO_6 . It confirmed that the MoS_2 QDs dispersed on the Bi_2WO_6 may form $p-n$ heterojunctions. The establishment of heterojunction is benefit of photogenerated electrons/holes separation, and as a result, the photocatalytic activity may be improved [4,13,14].

The photocatalytic kinetics of RhB degradation may be described using the Langmuir-Hinshelwood (L-H) model (Eq. (4)). The initial concentration of RhB in this work was set to approximately 10 mg/L ($\sim 2.1 \times 10^{-5}$ mol/L), so $(1 + K_c)$ may be assumed to be equal to 1. Eq. (5) may be expressed in the form of Eq. (6), where k' is the pseudo first-order rate constant. Integration of Eq. (6) then results in Eq. (7).

$$r = -\frac{dc}{dt} = k\theta = \frac{kK_c}{1 + K_c} \quad (5)$$

$$-\frac{dc}{dt} = kK_c = k'c \quad (6)$$

$$\ln\left(\frac{c_0}{c_t}\right) = k't \quad (7)$$

where r , c , t , k , θ , K , and k' represent reaction rate, concentration of RhB (c_0 : initial concentration; c_t : concentration at time t), time, reaction rate constant, ratio of adsorbed RhB, adsorption constant apparent reaction constant respectively. The apparent constants (k') can be obtained by fitting the plots of $\ln(c_0/c)$ vs t , which are summarized in Table 3. For the processes with pure MoS_2 and Bi_2WO_6 , the apparent reaction constant are 0.00421 and 0.01831 min^{-1} respectively. The introduction of MoS_2 greatly improved the reaction rate, and loading 1% of MoS_2 onto Bi_2WO_6 increased the constant up to 3 times that for bare Bi_2WO_6 . However, excessive MoS_2 onto Bi_2WO_6 hinders further increase of reaction constant, while it still higher than bare Bi_2WO_6 .

As for the step-by-step decomposition of RhB, it is explored by measuring the UV-vis spectra for samples taken during the degradation process. As shown in Fig. 9, the degradation process may incorporate two competitive processes as reported, namely the de-ethylation process and destruction of the conjugated structure [9,43]. Specifically, the blue-shift in wavelength from 554 to

Table 3

Apparent reaction kinetic constants of photocatalytic processes with different samples.

Composites	Bi_2WO_6	$x\% \text{MoS}_2\text{-Bi}_2\text{WO}_6$				MoS_2
		$x = 0.5$	$x = 1.0$	$x = 1.5$	$x = 2.0$	
$k' (\text{min}^{-1})$	0.01831	0.02114	0.05473	0.02841	0.02443	0.00421
$(k' - k'_{\text{Bi}_2\text{WO}_6})/k'_{\text{Bi}_2\text{WO}_6}$	0	0.15	2.00	0.55	0.33	-0.77
R^2	0.9876	0.9997	0.9845	0.9962	0.9982	0.9733

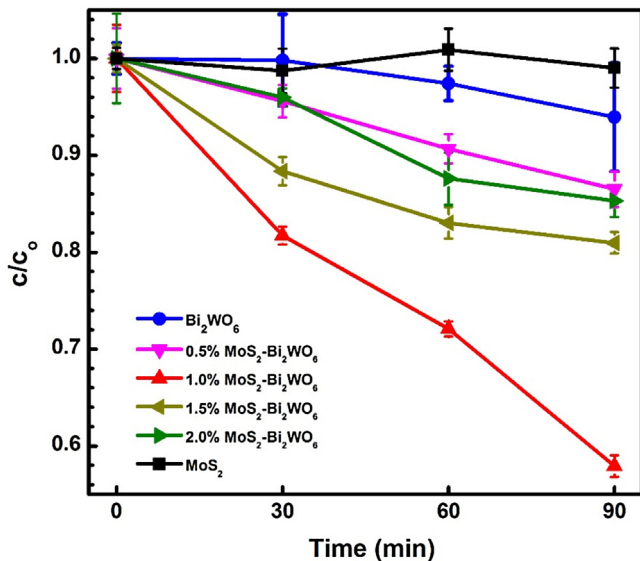


Fig. 10. Changes in TOC concentration during the course of photocatalytic degradation of RhB in the presence of prepared samples under visible light irradiation. (Catalyst dosages: 1 g/L, initial concentration of RhB: 10 mg/L, Temperature: 20 °C).

498 nm for characteristic peaks may be attributed to the RhB were transformed into rhodamine with intermediate products such as *N,N,N'-Triethyl-Rhodamine* (TER); *N,N-Diethyl-Rhodamine* (DER); *N-Ethyl-Rhodamine* (ER). In the first 40 min, the de-ethylation is the dominated process. After that, the destruction of aromatic ring becomes the dominated process. And rhodamine are degraded into small species such as CO_2 , H_2O , which is corresponding the intensity decrease until to none of the characteristic peak for rhodamine. This indicates RhB may be completely degraded into small species in the presence of $\text{MoS}_2\text{-Bi}_2\text{WO}_6$ under visible light for 90 min. Furthermore, the total organic carbon concentration during RhB photodegradation by prepared samples was measured and the results are illustrated in Fig. 10. It can be observed that the reduction rate of TOC is much slower than that of the dye; only 6% and 1% of TOC was reduced in the presence of pure Bi_2WO_6 and MoS_2 , respectively. It exhibited higher TOC reduction rate when MoS_2 was loaded on Bi_2WO_6 , and when the content of MoS_2 accounted for 1.0%, the mineralization yielded the maximum value of 42% in 90 min. This result is consistent with the decolorization result as shown in Fig. 9. Even though RhB was completely removed, it may be transformed into other organic compounds and longer time is required to achieve a complete photocatalytic mineralization of the dye.

The stability of $\text{MoS}_2\text{-Bi}_2\text{WO}_6$ composites during RhB degradation was investigated via recycling for four runs. The concentration profiles for each run are shown in Fig. 11. RhB were completely removed in 50 min for all runs, and a slight decrease was also observed in the initial degradation efficiency of RhB from the first run to fourth run. The decrease may be due to the catalyst loss in the processes of sampling and filtration. The negligible decrease in

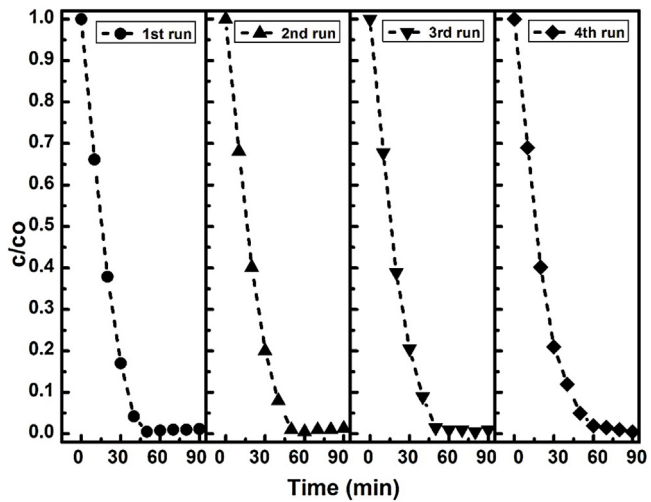


Fig. 11. Recycling 1.0% $\text{MoS}_2\text{-Bi}_2\text{WO}_6$ composites for four runs in the degradation of RhB under visible light irradiation.

the photocatalytic performance in RhB degradation indicates the high stability of as-prepared $\text{MoS}_2\text{-Bi}_2\text{WO}_6$ composites.

3.6.2. Temporal course of inactivation

The photocatalytic reactive oxidative species (ROS) interacting with the bacterial are able to result in the damage of the cell wall integrity, as the wall structural elements such as lipopolysaccharide, phosphatidylethanolcholine and peptidoglycan can be degraded by photocatalytic ROS [44,45]. When the integrity of the cell wall is damaged, it will alter the outer membrane permeability to allow the penetration of deleterious substances. The loss of membrane structure and function can result in bacterial death. To evaluate the temporal course of inactivation due to photocatalysis, a standard plate count method was used to quantify viable and cultivable bacterial concentration changes with time upon exposure to various treatments. A comparison of survival curves for dark control, photolysis and the prepared samples are shown in Fig. 12. The final survival ratio of $(80.0 \pm 1.96)\%$ was observed for the photolysis run, which represent cell death without any antibacterial, adsorptive or photocatalysis. For the dark control process, about $(83.5 \pm 7.41)\%$ of *E. coli* are survived, and the inactivation may be attributed to the adsorptive of the photocatalysts, suggesting the photocatalysts itself is not toxic to *E. coli*. For pure MoS_2 and Bi_2WO_6 trials, final survival ratios of $(75.0 \pm 3.59)\%$ and $(49.8 \pm 2.72)\%$ respectively are found. Via coupling MoS_2 with Bi_2WO_6 , only $(6.7 \pm 3.53)\%$ of *E. coli* are survived owing for the enhanced photocatalytic effect. The significant decrease in population of *E. coli* in solution under visible light may be resulted from the improved separation efficiency of photogenerated electrical carriers after the formation of $\text{MoS}_2\text{-Bi}_2\text{WO}_6$ *p-n* heterojunction. The results are in good agreement with the photocatalytic degradation of RhB. The treated waters were stored for three days to investigate the bacterial regrowth. The fact that no apparent regrowth

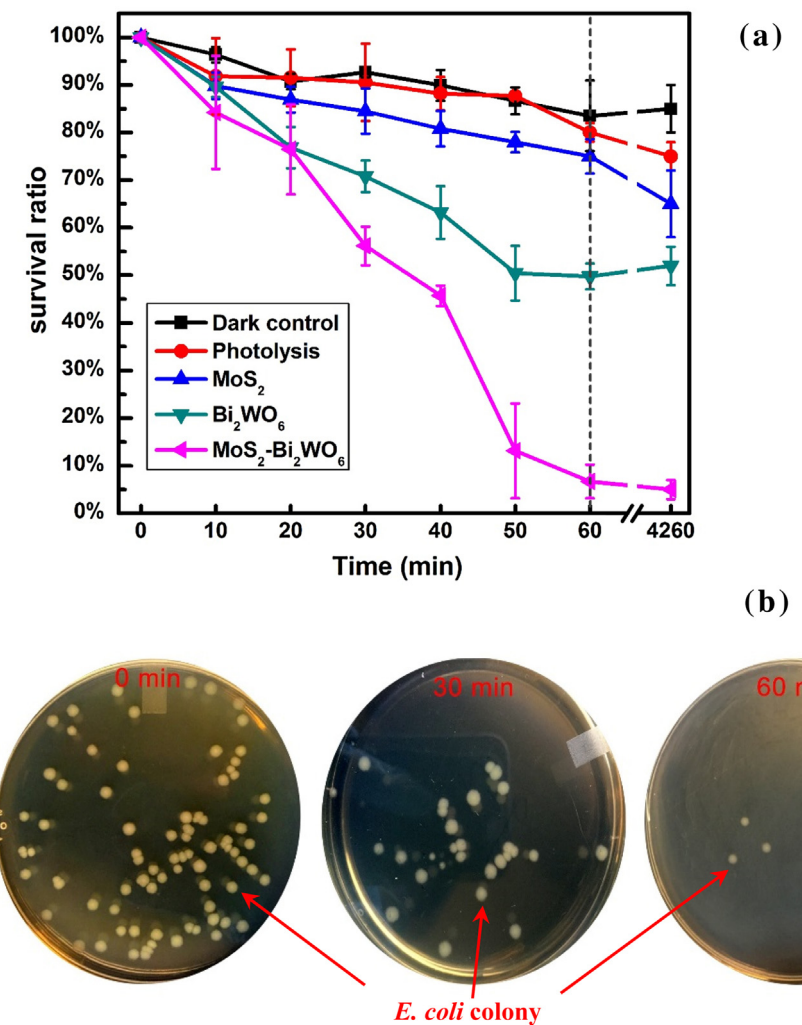


Fig. 12. (a) Inactivation curves for dark control, photolysis and irradiated composite; (b) photos of *E. coli* colonies on an agar plate for samples taken and spread at different time during the photocatalytic disinfection in the presence of 1%MoS₂-Bi₂WO₆.

were found after 3-day storage suggests that the bacteria were completely inactivated via the photocatalysis.

3.7. Electrochemical exploration

To explore the electrochemical property, especially the interface charge separation efficiency, electrochemical impedance spectroscopy (EIS) was measured and the EIS Nyquist plots of Bi₂WO₆ as well as MoS₂-Bi₂WO₆ composites under visible light irradiation are shown in Fig. 13. Only one semicircle is observed for each EIS Nyquist plot, indicates these photocatalysis process in the presence of prepared samples may be a simple electrode reaction. And the photogenerated electrical carriers transfer rate is able to be determined by their recombination rate [46,47]. Based on plots shown in Fig. 13, the equivalent circuit and the fitted electrical parameters for each process are summarized in Table 4. Specifically, R_s is the resistance of the solution, R_{ct} is the resistance to electron transfer and CPE represents the constant phase element, which may be considered as a double-layered capacitor. The diameter of the arc in the EIS Nyquist plot determines the R_{ct} , where larger diameters resulting in higher values for R_{ct} and lower electrons transfer rate [48]. It can be observed, processes with MoS₂-Bi₂WO₆ exhibit smaller resistance compared to that of bare Bi₂WO₆ which is 328.5 kΩ. And when the introduction of MoS₂ with the quantity increase from 0.5% to 1%, the R_{ct} value is decreased from 30.4 to 18.1 kΩ. How-

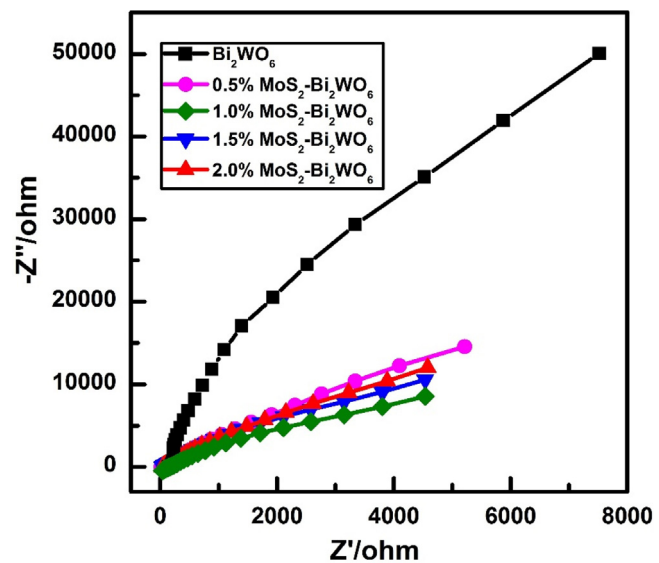


Fig. 13. EIS Nyquist plots of the Bi₂WO₆ and MoS₂-Bi₂WO₆ photocatalysts.

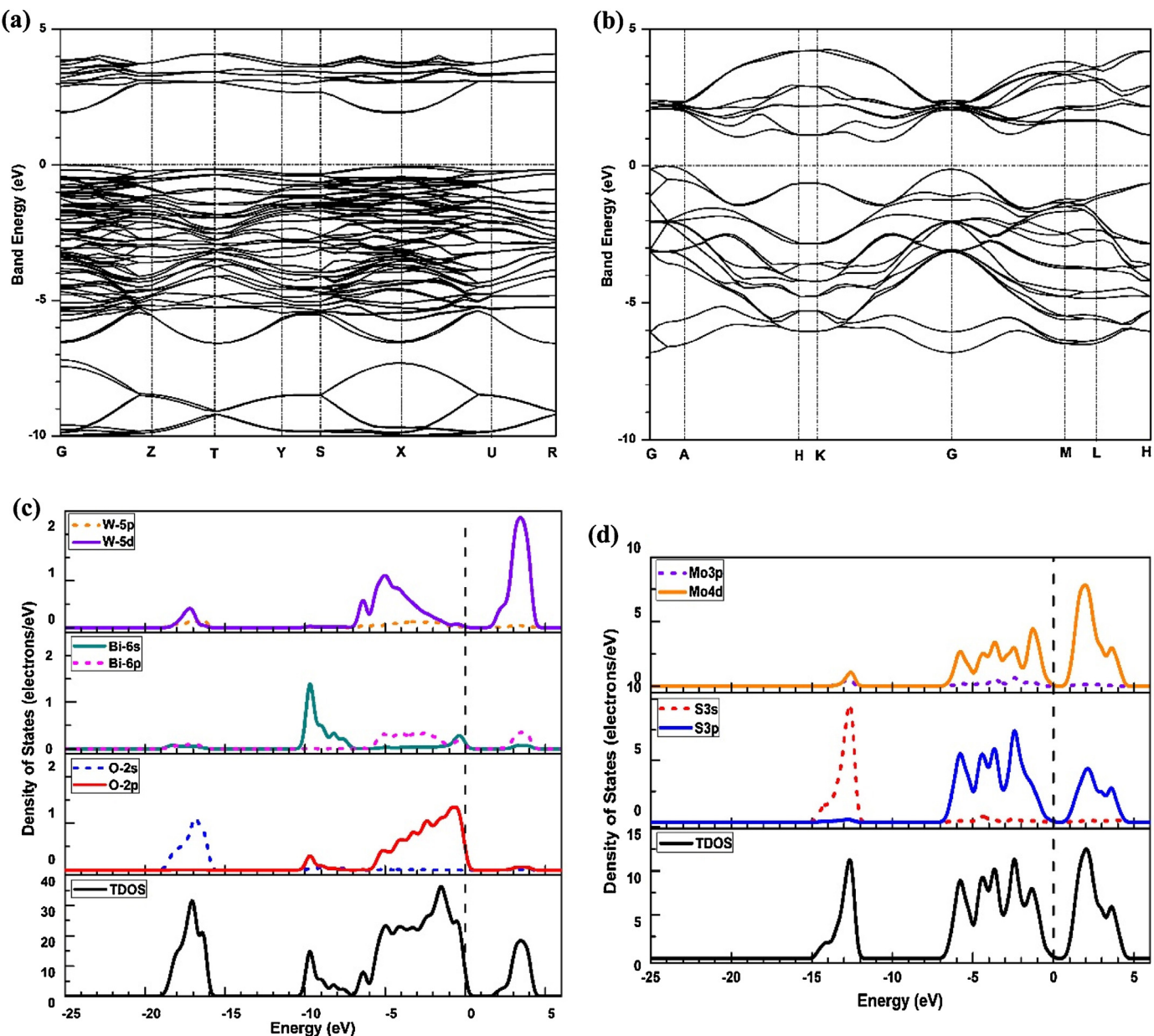


Fig. 14. (a, b) Band structure for Bi₂WO₆ and MoS₂. (c, d) Partial and total density of states (PDOS and TDOS) for Bi₂WO₆ and MoS₂. (Simulated by Quantum Espresso [29]).

Table 4

Fitting results for equivalent circuits of different prepared samples.

Samples	R _s (Ω)	R _{ct} ($k\Omega$)	CPE (μF)	Equivalent circuits
Bi ₂ WO ₆	165.8	328.5	41.6	
0.5%MoS ₂ -Bi ₂ WO ₆	154.1	30.4	59.9	
1.0%MoS ₂ -Bi ₂ WO ₆	125.5	18.1	83.1	
1.5%MoS ₂ -Bi ₂ WO ₆	141.9	27.8	55.0	
2.0%MoS ₂ -Bi ₂ WO ₆	167.4	26.1	36.1	

ever, further increase the loading amount of MoS₂ higher than 1%, the R_{ct} is increase to 27.8 k Ω for 1.5%MoS₂-Bi₂WO₆ and 26.1 k Ω for 2.0% MoS₂-Bi₂WO₆. It suggests the introduction of MoS₂ QDs on Bi₂WO₆ can greatly improve the separation of photogenerated electron/hole pairs, and when the quantity of MoS₂ account for 1.0%, the electron/hole separation efficiency is the highest. It is a crucial evidence to confirm that the introduction MoS₂ on Bi₂WO₆ can significantly improve the electron/hole separation efficiency and further enhanced the photocatalytic activity in the removal of

organic pollutants as well as bacterial inactivation under visible light irradiation.

3.8. Energy band engineering analysis

Band structures and partial/total density of states (PDOS/TDOS) for Bi₂WO₆ and MoS₂ are simulated based on DFT method and illustrated in Fig. 14. The energy of top of valence band is fixed at zero. The band gap value (Fig. 14a and b) can be measured as

Table 5

Band gap and flat-band edge position of Bi_2WO_6 and MoS_2 .

Composites	E_g/eV	χ_p/eV	E^e/eV	E_{CB} vs NHE ^a /eV	E_{VB} vs NHE ^a /eV
Bi_2WO_6	2.70	6.20	4.50	0.35	3.05
MoS_2	1.30 ^b	5.33	4.50	0.18	1.48

a. NHE: Normal Hydrogen Electrode; b. For bulk MoS_2 , band gap is 1.30 eV (adapted from [49]).

about 1.91 eV for Bi_2WO_6 and 0.89 eV for MoS_2 . The simulated band gap values are narrower than experimental results (2.70 eV for Bi_2WO_6 and 1.3 eV for bulk MoS_2 [49]), which may be resulted from the well-known limitation of GGA [50]. It can be found the Bi_2WO_6 is attributed to the direct band-gap semiconductor and MoS_2 is attributed to indirect band-gap semiconductor. It should also be noted the correlation between velocity of electron (v) and the energy of electron E can be expressed as in Eq. (8).

$$v = \frac{\Delta_k E(\kappa)}{\hbar} \quad (8)$$

It means that the more flat the energy band is, the more localized the charge carriers [51]. For Bi_2WO_6 , the mobility of both electrons and holes are relatively low, which inevitably inhibit the separation efficiency of photogenerated electrical carriers. It indicates even for a 'perfect' bulk Bi_2WO_6 , the photocatalytic activity can still be significantly improved in photocatalysis. From the PDOS/DOS shown in Fig. 14c and d, the valence band of Bi_2WO_6 is composed of O 2p, W 5d and a little Bi 6s. As reported the well-dispersed Bi 6s orbital facilitate the mobility of photogenerated carriers and narrows the band gap [3,4]. The top valence band of MoS_2 mainly originated from the 4d orbital of Mo and 3p orbital of S, and the bottom of MoS_2 is mainly contributed to 4d orbitals of Mo.

To further study photogenerated electrons and holes transfer when MoS_2 - Bi_2WO_6 composite applied in photocatalysis, The flat-band potentials of semiconductors can be calculated by applying the Mulliken electronegativity theory for atoms as follows (Eqs. (9) and (10)) [1,52],

$$E_{CB} = \chi_p - E^e - \frac{1}{2}E_g \quad (9)$$

$$E_{VB} = E_{CB} + E_g \quad (10)$$

where E_{CB} and E_{VB} are bottom position of conduction band and top position of valence band respectively; χ_p represents the electronegativity which can be estimated by the geometric mean of electronegativity of the constituent atoms [53–55]; E^e is the energy of free electrons on the hydrogen scale (~4.5 eV) and E_g is the band gap value. The calculated results for Bi_2WO_6 and MoS_2 are summarized in Table 5, and the flat-band position for MoS_2 - Bi_2WO_6 is schemed in Fig. 15. A staggered type II band alignment and a built-in electric field formed near the interface. The formation MoS_2 - Bi_2WO_6 p-n heterojunction facilitate the separation of photogenerated electrons and holes. The built-in electric field may drive the mobility of electrons from conduction band of MoS_2 to that of Bi_2WO_6 , while holes transferred from the valence band of Bi_2WO_6 to that of MoS_2 . As a result, electrons and holes are accumulated on Bi_2WO_6 and MoS_2 separately. It is also reported that QDs combined on a photocatalysts may provide a convenient way to direct the flow of the photogenerated charge carriers [24,25]. Fast electron transfer between MoS_2 QDs and Bi_2WO_6 may lead to higher quantum efficiency, providing more photogenerated electrons utilized in photocatalytic reactions. The surface OH or H_2O capture the separated holes at the surface of the photocatalysts and produce hydroxyl free radicals ($\cdot\text{OH}$). Besides, the dissolved O_2 can also react with the separated electrons to generate superoxide free radicals ($\cdot\text{O}_2^-$) or hydroperoxyl radicals ($\cdot\text{O}_2\text{H}$). The generated free radicals as well as the photogenerated holes are

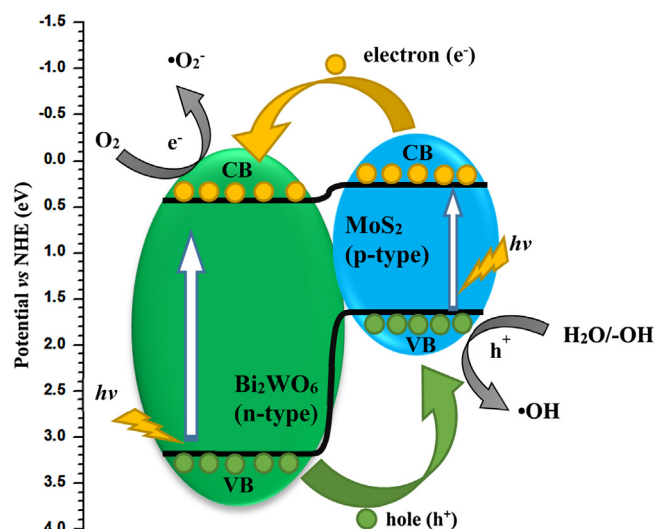


Fig. 15. Proposed mechanism of photogenerated electrons and holes transfer for MoS_2 - Bi_2WO_6 composite under visible light irradiation.

oxidative enough to effectively decompose the organic pollutants and damage the cell envelope integrity.

4. Conclusions

MoS_2 QDs interspersed- Bi_2WO_6 heterostructure was successfully prepared via a simple bath sonication method. Characterizations are performed and suggest hexagonal MoS_2 QDs with size of 1.8–5.6 nm are interspersed on Bi_2WO_6 nanoplates. The band gap of Bi_2WO_6 is 2.70 eV, and the band gap is narrowed after MoS_2 QDs loading on its surface. The adsorption capacity is significantly improved with introduction of MoS_2 , compared to bare Bi_2WO_6 . Moreover, in the photocatalytic RhB degradation and the temporal course of inactivation, MoS_2 - Bi_2WO_6 exhibit enhanced photocatalytic activity compared to bare Bi_2WO_6 and MoS_2 . The synergy effect on photocatalysis oxidation may be attributed to the p-n heterojunction between MoS_2 and Bi_2WO_6 , as well as the MoS_2 QDs facilitate the charge carrier separation. This work is a crucial evidence to confirm MoS_2 QDs as a promising co-catalyst in preparation of an efficient photocatalyst.

Acknowledgements

This work was financially supported by the Natural Sciences and Engineering Research Council of Canada. Xiangchao Meng and Zizhen Li were the recipients of a scholarship from the China Scholarship Council for the duration of this work. The authors would like to acknowledge Drs. Alexander Mommers, Yong Yang and Yun Liu at the Center for Catalysis Research and Innovation (CCRI at University of Ottawa) and Patrick M. D'Aoust (Laboratory Technician, Environmental Engineering at University of Ottawa) for their helps with material characterizations.

References

- [1] X. Meng, Z. Zhang, Bismuth-based photocatalytic semiconductors: introduction, challenges and possible approaches, *J. Mol. Catal. A: Chem.* 423 (2016) 533–549.
- [2] R.a. He, S. Cao, P. Zhou, J. Yu, Recent advances in visible light Bi-based photocatalysts, *Chin. J. Catal.* 35 (2014) 989–1007.
- [3] H. An, Y. Du, T. Wang, C. Wang, W. Hao, J. Zhang, Photocatalytic properties of BiOX ($X = \text{Cl}, \text{Br}$, and I), *Rare Met.* 27 (2008) 243–250.
- [4] X. Meng, Z. Zhang, Facile synthesis of $\text{BiOBr}/\text{Bi}_2\text{WO}_6$ heterojunction semiconductors with high visible-light-driven photocatalytic activity, *J. Photochem. Photobiol. A: Chem.* 310 (2015) 33–44.

[5] C. Zhang, Y. Zhu, Synthesis of square Bi_2WO_6 nanoplates as high-activity visible-light-driven photocatalysts, *Chem. Mater.* 17 (2005) 3537–3545.

[6] L. Zhang, W. Wang, L. Zhou, H. Xu, Bi_2WO_6 nano-and microstructures: shape control and associated visible-light-driven photocatalytic activities, *Small* 3 (2007) 1618–1625.

[7] Y. Huang, Z. Ai, W. Ho, M. Chen, S. Lee, Ultrasonic spray pyrolysis synthesis of porous Bi_2WO_6 microspheres and their visible-light-induced photocatalytic removal of NO, *J. Phys. Chem. C* 114 (2010) 6342–6349.

[8] X. Hu, X. Meng, Z. Zhang, Synthesis and characterization of graphene oxide-modified Bi_2WO_6 and its use as photocatalyst, *Int. J. Photoenergy* 2016 (2016) 8.

[9] H. Fu, S. Zhang, T. Xu, Y. Zhu, J. Chen, Photocatalytic degradation of RhB by fluorinated Bi_2WO_6 and distributions of the intermediate products, *Environ. Sci. Technol.* 42 (2008) 2085–2091.

[10] Y. Fu, C. Chang, P. Chen, X. Chu, L. Zhu, Enhanced photocatalytic performance of boron doped Bi_2WO_6 nanosheets under simulated solar light irradiation, *J. Hazard. Mater.* 254–255 (2013) 185–192.

[11] L. Ge, C. Han, J. Liu, Novel visible light-induced $\text{G-C}_3\text{N}_4/\text{Bi}_2\text{WO}_6$ composite photocatalysts for efficient degradation of methyl orange, *Appl. Catal. B: Environ.* 108–109 (2011) 100–107.

[12] M. Ge, Y. Li, L. Liu, Z. Zhou, W. Chen, $\text{Bi}_2\text{O}_3\text{-Bi}_2\text{WO}_6$ composite microspheres: hydrothermal synthesis and photocatalytic performances, *J. Phys. Chem. C* 115 (2011) 5220–5225.

[13] X. Meng, L. Jiang, W. Wang, Z. Zhang, Enhanced photocatalytic activity of BiOBr/ZnO heterojunction semiconductors prepared by facile hydrothermal method, *Int. J. Photoenergy* 2015 (2015) 9.

[14] X. Meng, Z. Zhang, Synthesis, analysis, and testing of $\text{BiOBr}\text{-Bi}_2\text{WO}_6$ photocatalytic heterojunction semiconductors, *Int. J. Photoenergy* 2015 (2015) 12.

[15] Q. Xiang, J. Yu, M. Jaroniec, Graphene-based semiconductor photocatalysts, *Chem. Soc. Rev.* 41 (2012) 782–796.

[16] S. Cao, J. Yu, $\text{G-C}_3\text{N}_4$ -based photocatalysts for hydrogen generation, *J. Phys. Chem. Lett.* 5 (2014) 2101–2107.

[17] Q. Li, N. Zhang, Y. Yang, G. Wang, D.H.L. Ng, High efficiency photocatalysis for pollutant degradation with $\text{MoS}_2/\text{C}_3\text{N}_4$ heterostructures, *Langmuir* 30 (2014) 8965–8972.

[18] S. Bai, L. Wang, X. Chen, J. Du, Y. Xiong, Chemically exfoliated metallic MoS_2 nanosheets: a promising supporting co-catalyst for enhancing the photocatalytic performance of TiO_2 nanocrystals, *Nano Res.* 8 (2015) 175–183.

[19] T.F. Jaramillo, K.P. Jørgensen, J. Bonde, J.H. Nielsen, S. Horch, I. Chorkendorff, Identification of active edge sites for electrochemical H_2 evolution from MoS_2 nanocatalysts, *Science* 317 (2007) 100–102.

[20] J. Xie, J. Zhang, S. Li, F. Grote, X. Zhang, H. Zhang, R. Wang, Y. Lei, B. Pan, Y. Xie, Controllable disorder engineering in oxygen-incorporated MoS_2 ultrathin nanosheets for efficient hydrogen evolution, *J. Am. Chem. Soc.* 135 (2013) 17881–17888.

[21] J. Zhang, L. Huang, H. Jin, Y. Sun, X. Ma, E. Zhang, H. Wang, Z. Kong, J. Xi, Z. Ji, Constructing two-dimension $\text{MoS}_2/\text{Bi}_2\text{WO}_6$ core-shell heterostructure as carriers transfer channel for enhancing photocatalytic activity, *Mater. Res. Bull.* 85 (2017) 140–146.

[22] F. Wang, W. Li, S. Gu, H. Li, X. Wu, C. Ren, X. Liu, Facile fabrication of direct Z-scheme $\text{MoS}_2/\text{Bi}_2\text{WO}_6$ heterojunction photocatalyst with superior photocatalytic performance under visible light irradiation, *J. Photochem. Photobiol. A: Chem.* 335 (2017) 140–148.

[23] D. Gopalakrishnan, D. Damien, M.M. Shajumon, MoS_2 quantum dot-interspersed exfoliated MoS_2 nanosheets, *ACS Nano* 8 (2014) 5297–5303.

[24] H. Zhang, H. Huang, H. Ming, H. Li, L. Zhang, Y. Liu, Z. Kang, Carbon quantum dots/ Ag_3PO_4 complex photocatalysts with enhanced photocatalytic activity and stability under visible light, *J. Mater. Chem.* 22 (2012) 10501–10506.

[25] G.-S. Li, D.-Q. Zhang, J.C. Yu, A new visible-light photocatalyst: CdS quantum dots embedded mesoporous TiO_2 , *Environ. Sci. Technol.* 43 (2009) 7079–7085.

[26] Y.-H. Tan, K. Yu, J.-Z. Li, H. Fu, Z.-Q. Zhu, $\text{MoS}_2@\text{ZnO}$ nano-heterojunctions with enhanced photocatalysis and field emission properties, *J. Appl. Phys.* 116 (2014) 064305.

[27] J. Gamage McEvoy, D.A. Bilodeau, W. Cui, Z. Zhang, Visible-light-driven inactivation of *Escherichia coli* K-12 using an Ag/AgCl -activated carbon composite photocatalyst, *J. Photochem. Photobiol. A: Chem.* 267 (2013) 25–34.

[28] W. Kohn, L.J. Sham, Self-consistent equations including exchange and correlation effects, *Phys. Rev.* 140 (1965) A1133.

[29] G. Paolo, B. Stefano, B. Nicola, C. Matteo, C. Roberto, C. Carlo, C. Davide, L.C. Guido, C. Matteo, D. Ismaila, C. Andrea Dal, G. Stefano de, F. Stefano, F. Guido, G. Ralph, G. Uwe, G. Christos, K. Anton, L. Michele, M.-S. Layla, M. Nicola, M. Francesco, M. Riccardo, P. Stefano, P. Alfredo, P. Lorenzo, S. Carlo, S. Sandro, S. Gabriele, P.S. Ari, S. Alexander, U. Paolo, M.W. Renata, QUANTUM ESPRESSO: a modular and open-source software project for quantum simulations of materials, *J. Phys.: Condens. Matter* 21 (2009) 395502.

[30] K.S. Knight, The crystal structure of russellite; a re-determination using neutron powder diffraction of synthetic BhW_06 , (1992).

[31] T. Xiong, M. Wen, F. Dong, J. Yu, L. Han, B. Lei, Y. Zhang, X. Tang, Z. Zang, Three dimensional Z-scheme $(\text{BiO})_2\text{CO}_3/\text{MoS}_2$ with enhanced visible light photocatalytic NO removal, *Appl. Catal. B: Environ.* 199 (2016) 87–95.

[32] Y. Xu, H. Xu, H. Li, J. Xia, C. Liu, L. Liu, Enhanced photocatalytic activity of new photocatalyst $\text{Ag}/\text{AgCl}/\text{ZnO}$, *J. Alloys Compd.* 509 (2011) 3286–3292.

[33] Z. Shuxian, W.K. Hall, G. Ertl, H. Knözinger, X-ray photoemission study of oxygen and nitric oxide adsorption on MoS_2 , *J. Catal.* 100 (1986) 167–175.

[34] H.W. Wang, P. Skeldon, G.E. Thompson, XPS studies of MoS_2 formation from ammonium tetrathiomolybdate solutions, *Surf. Coat. Technol.* 91 (1997) 200–207.

[35] T.A. Patterson, J.C. Carver, D.E. Leyden, D.M. Hercules, A surface study of cobalt-molybdena-alumina catalysts using x-ray photoelectron spectroscopy, *J. Phys. Chem.* 80 (1976) 1700–1708.

[36] C.D. Wagner, Sensitivity of detection of the elements by photoelectron spectrometry, *Anal. Chem.* 44 (1972) 1050–1053.

[37] J. Li, Z. Guo, Y. Wang, Z. Zhu, Three-dimensional $\text{TiO}_2/\text{Bi}_2\text{WO}_6$ hierarchical heterostructure with enhanced visible photocatalytic activity, *Micro Nano Lett.* 9 (2014) 65–68.

[38] K. Sing, D. Everett, R. Haul, L. Moscou, R. Pierotti, J. Rouquerol, T. Siemieniewska, Physical and biophysical chemistry division commission on colloid and surface chemistry including catalysis, *Pure Appl. Chem.* 57 (1985) 603–619.

[39] M. Kruck, M. Jaroniec, Gas adsorption characterization of ordered organic-inorganic nanocomposite materials, *Chem. Mater.* 13 (2001) 3169–3183.

[40] X. Meng, Z. Zhang, Plasmonic ternary $\text{Ag}-\text{rGO}-\text{Bi}_2\text{MoO}_6$ composites with enhanced visible light-driven photocatalytic activity, *J. Catal.* 344 (2016) 616–630.

[41] H. Yuh-Shan, Citation review of Lagergren kinetic rate equation on adsorption reactions, *Scientometrics* 59 (2004) 171–177.

[42] M. Özçar, Equilibrium and kinetic modelling of adsorption of phosphorus on calcined alunite, *Adsorption* 9 (2003) 125–132.

[43] T. Watanabe, T. Takizawa, K. Honda, Photocatalysis through excitation of adsorbates. 1. Highly efficient N-deethylation of rhodamine B adsorbed to cadmium sulfide, *J. Phys. Chem.* 81 (1977) 1845–1851.

[44] J. Kiwi, V. Nadtochenko, Evidence for the mechanism of photocatalytic degradation of the bacterial wall membrane at the TiO_2 interface by ATR-FTIR and laser kinetic spectroscopy, *Langmuir* 21 (2005) 4631–4641.

[45] S. Piget-Rémy, F. Simonet, E. Errazuriz-Cerdá, J.C. Lazzaroni, D. Atlani, C. Guillard, Photocatalysis and disinfection of water: identification of potential bacterial targets, *Appl. Catal. B: Environ.* 104 (2011) 390–398.

[46] J.M. Kesselman, G.A. Shreve, M.R. Hoffmann, N.S. Lewis, Flux-matching conditions at TiO_2 photoelectrodes: is interfacial electron transfer to O_2 rate-limiting in the TiO_2 -catalyzed photochemical degradation of organics? *J. Phys. Chem.* 98 (1994) 13385–13395.

[47] B. Xin, Z. Ren, H. Hu, X. Zhang, C. Dong, K. Shi, L. Jing, H. Fu, Photocatalytic activity and interfacial carrier transfer of $\text{Ag}-\text{TiO}_2$ nanoparticle films, *Appl. Surf. Sci.* 252 (2005) 2050–2055.

[48] B. Xin, Z. Ren, P. Wang, J. Liu, L. Jing, H. Fu, Study on the mechanisms of photoinduced carrier separation and recombination for $\text{Fe}^{3+}-\text{TiO}_2$ photocatalysts, *Appl. Surf. Sci.* 253 (2007) 4390–4395.

[49] K.F. Mak, C. Lee, J. Hone, J. Shan, T.F. Heinz, Atomically thin MoS_2 : a new direct-gap semiconductor, *Phys. Rev. Lett.* 105 (2010) 136805.

[50] K. Lai, W. Wei, Y. Dai, R. Zhang, B. Huang, DFT calculations on structural and electronic properties of Bi_2MO_6 ($\text{M} = \text{Cr}, \text{Mo}, \text{W}$), *Rare Met.* 30 (2011) 166–172.

[51] H. Li, K. Yu, X. Lei, B. Guo, H. Fu, Z. Zhu, Hydrothermal synthesis of novel $\text{MoS}_2/\text{BiVO}_4$ hetero-nanoflowers with enhanced photocatalytic activity and a mechanism investigation, *J. Phys. Chem. C* 119 (2015) 22681–22689.

[52] Y. Xu, M.A.A. Schoonen, The absolute energy positions of conduction and valence bands of selected semiconducting minerals, *Am. Mineral.* 85 (2000) 543–556.

[53] R.T. Sanderson, *Chemical Periodicity*, Reinhold, New York, US, 1961.

[54] R.S. Mulliken, A new electroaffinity scale; together with data on valence states and on valence ionization potentials and electron affinities, *J. Chem. Phys.* 2 (1934) 782–793.

[55] R.S. Mulliken, Electronic structures of molecules XI. Electroaffinity, molecular orbitals and dipole moments, *J. Chem. Phys.* 3 (1935) 573–585.